https://doi.org/10.5194/egusphere-2026-978
Preprint. Discussion started: 4 March 2026

Current status of ocean observation, ensemble reanalysis and CMIP6 models in describing Antarctic Bottom Water

Siran Chen[1], Jiping Liu*[1] and Xianxian Han[1]

[1]School of Atmospheric Sciences, Sun Yat-sen University and Southern Marine Science and Engineering Guangdong Laboratory (Zhuhai), Zhuhai, China

*Corresponding author: Jiping Liu (liujp63@mail.sysu.edu.cn)

Abstract

Antarctic Bottom Water (AABW), a key component of the global meridional overturning circulation, forms in distinct regions around Antarctic coasts. The properties of AABW from different sources can be distinguished by their temperature and salinity properties. This study proposes a classification scheme to divide AABW into three subtypes based on their properties and geographic regions: Weddell Sea and Prydz Bay-originated AABW (WPBW), Ross Sea-originated AABW (RSBW), and Adélie Land-originated AABW (ALBW). These three subtypes are clearly identified in the World Ocean Atlas 2023 (WOA23) dataset. Taking WOA23 as a benchmark, we then systematically evaluate the ability of other datasets, including ensemble ocean reanalysis and CMIP6 models, to represent the spatial distribution and thermohaline properties of these AABW subtypes. Results indicate that the ensemble reanalysis performs well, albeit with an overestimation of ALBW. Nearly all CMIP6 models fail to capture these AABW subtypes, except after the correction of systematic temperature and salinity biases. Notably, CESM1-CAM5-SE-LR is the only model reproducing the three AABW subtypes without the correction, likely due to that the implemented overflow parameterization fits tuned physical processes. Comparison with its high resolution counterpart indicates that increased model resolution may not necessarily improve AABW simulations. This refined classification framework, along

https://doi.org/10.5194/egusphere-2026-978
Preprint. Discussion started: 4 March 2026

with the evaluation of various datasets, provides a foundation for more detailed investigations into the AABW formation, variability, and trends under climate change.

1 Introduction

Antarctic Bottom Water (AABW) is the coldest and densest water mass in the global ocean. AABW is primarily sourced from coastal polynyas and extends across most of the world's oceans, constituting approximately 30–40 % of the global ocean volume (Johnson et al., 2008) . As the principal driver of the lower limb of the global meridional overturning circulation (Orsi et al., 1999), the formation and transport of AABW significantly influence vertical redistribution of heat (Purkey & Johnson, 2010) and ocean's capacity for long term carbon sequestration (Burke & Robinson, 2012; Marinov et al., 2006; Zhang et al., 2023) . Therefore, understanding the generation and variability of AABW is crucial for assessing oceanic heat budgets and biogeochemical cycles under the background of global warming. However, in-situ observations of AABW remain limited due to the extensive sea ice cover and extreme climatic conditions over the Antarctic continental shelf and slope regions. Furthermore, because AABW predominantly resides at depths exceeding 2000 meters, its characterization using satellites or conventional buoys remains very challenging (Silvano et al., 2023).

Observational data form the foundation for AABW research. While data from key transects can accurately reflect AABW properties in specific regions, they are sparse, temporally discontinuous, and subject to systematic biases (Purkey & Johnson, 2013). In contrast, the World Ocean Atlas 2023 (WOA23) integrates nearly all historical marine observations with rigorous quality control. Although it attenuates small-scale, regional, and transient signals due to smoothing and averaging, WOA23 is well suited for representing the large-scale, long-term averaged climatic state of AABW. However, investigating the variability and trends of AABW is becoming increasingly

https://doi.org/10.5194/egusphere-2026-978
Preprint. Discussion started: 4 March 2026

important, especially under global warming. In this context, ocean reanalysis products and climate models also provide valuable datasets.

Several ocean reanalysis products are used to study AABW. Among them, ECCO2 can generally reproduce the upper bounds of AABW (defined by a density threshold $\gamma^n \geq 28.27$ kg m^{-3}) (Azaneu et al., 2014) , but the post-2004 ECCO2 exhibits unrealistic open-ocean polynyas and deep convection in the Weddell Sea region, failing to capture the Weddell Sea Bottom Water (WSBW) (Azaneu et al., 2014) . GECCO2 shows a substantial fresh bias throughout the water column, whereas GLORYS2v4 and GloSea5-GO5 are generally saltier in certain layers. Taken together, the multi-model ensemble mean provides the best agreement with observations (Uotila et al., 2019). In addition to reanalysis products, global climate models such as those from the Coupled Model Intercomparison Project Phase 6 (CMIP6) are increasingly used to study AABW. However, only a few CMIP6 models can simulate the shelf overflow processes, with most relying instead on open-ocean deep convection, particularly in the Weddell and Ross Seas. As a result, the multi-model mean AABW is generally warmer, fresher, and lighter than observations (Heuzé, 2021). These issues highlight the necessity of evaluating the ability of reanalysis and climate model datasets to represent AABW.

The Weddell Sea, Ross Sea, Adélie Coast, and Prydz Bay are widely recognized as the four primary source regions of AABW (Gordon et al., 1993; Ohshima et al., 2013; Silvano et al., 2023; Williams et al., 2008). However, significant differences exist in the key physical processes governing AABW formation across these regions. These include variations in basal ice-shelf melt rates, sea-ice production rates, the intensity and direction of prevailing wind fields, and oceanic dynamical processes (e.g., overflows and mixing) (Han et al., 2024, 2025; Pardo et al., 2012; Schmidt et al., 2023; Silvano et al., 2018, 2023) . Such differences lead to distinct regional characteristics in the initial temperature and salinity signatures of the source water, and consequently to marked differences in AABW properties in the deep ocean (Orsi et al., 1999; Silvano et al., 2023). Many large-scale studies conventionally approach

AABW as a broadly uniform water mass. While this provides a useful framework for global analysis, it may not fully capture the significant physical variations that exist across different regions (Rintoul, 2018; Zhang et al., 2023), as AABW originating from different source regions exhibit distinct thermohaline properties. These differences might lead to variations in their respective contributions to global oceanic thermodynamic processes, such as patterns of abyssal warming and changes in overturning circulation intensity, as well as in their capacities for carbon uptake and storage.

To address this, this study proposes a refined definition for further classifying AABW. Taking WOA23 as a benchmark, we characterize the spatial distribution and thermohaline properties of AABW subtypes. Furthermore, we evaluate the capabilities and deficiencies of ocean reanalysis products and global climate models in representing these AABW subtypes. This new classification framework is intended to provide a foundation for subsequent, more detailed investigations into the formation mechanisms, distinctive characteristics, and variability and impacts of AABW originating from different source regions.

2 Data and Methods

2.1 Data

2.1.1 Observational Data.

This study utilizes full-depth ocean temperature and salinity climatological objective analysis fields from WOA23 (Reagan et al., 2024; Locarnini et al., 2024), covering the period 1991–2020. The data are provided on a 1/4° latitude-longitude grid with 102 vertical levels. WOA23 is a global ocean climatology product developed and distributed by the National Centers for Environmental Information of the National Oceanic and Atmospheric Administration. The dataset integrates measurements from multiple observational platforms and has undergone rigorous quality control procedures. These include removal of duplicate records, range and gradient checks, statistical significance testing based on 3–5 standard deviation thresholds, hydrostatic stability verification, and manual flagging of suspicious values. In addition, uncorrected real-time Argo salinity data have been excluded. To address the warm bias associated with Expendable Bathythermograph (XBT) and Mechanical Bathythermograph (MBT) measurements relative to bottle/CTD temperature data (Gouretski & Koltermann, 2007) , the bias correction scheme (Cheng et al., 2014; Levitus et al., 2009) is applied. For salinity, the initial quality-controlled profiles are interpolated to standard depth levels using the Reiniger–Ross method, followed by the objective analysis via the Barnes scheme. To mitigate spurious vertical density instabilities arising from inconsistencies between temperature and salinity profiles, often due to the greater abundance of temperature observations, a joint stabilization algorithm (Jackett & Mcdougall, 1995) is applied. This procedure ensures that the final temperature and salinity fields yield a hydrostatically stable water column.

2.1.2 Reanalysis Data.

This study utilizes the ensemble mean of sea water potential temperature and salinity from 1993 to 2022, derived from Global Ocean Ensemble Physics Reanalysis (Product ID: GLOBAL-MULTIYEAR-PHY-ENS-001-031) provided by the Copernicus Marine Service. This dataset integrates outputs from three independent ocean reanalysis systems: GLORYS2V4 (Mercator Ocean; Lellouche et al., 2013) , ORAS5 (ECMWF; Zuo et al., 2019) , and C-GLORSv5 (CMCC; Storto & Masina, 2016) . It delivers monthly averaged variables, including sea water temperature, salinity, current velocity, and sea surface height, from 1993 onward, at a horizontal resolution of 0.25° and with 75 vertical layers. The production system is based on the NEMO ocean model and the ORCA025 grid, forced by ERA-Interim and ERA5 atmospheric fields. Multi-source observational data are assimilated, encompassing sea level anomalies (SLA), sea surface temperature (SST), sea ice concentration (SIC), and in situ temperature/salinity (T/S) profiles. The ensemble is constructed via post-processing of the three reanalysis members, which differ in their model versions, surface forcing treatments, and data assimilation schemes. This diversity enhances the robustness and stability of the ensemble estimates.

2.1.3 Model outputs

This study utilizes data from 16 CMIP6 models, selected based on the availability of either the "historical" experiment or the "hist-1950" experiment and on the condition that monthly output for sea water salinity and potential temperature was accessible as of the data retrieval cutoff date. All selected models provide output on standard z-coordinates. Only the AWI-CM-1-1-HR dataset has a shorter period (1993–2010) compared to the others (1993–2014). Details of each model are provided in Table 1.

Table 1. Key characteristics of the 16 CMIP6 models utilized in this study, including their ocean component, nominal horizontal resolution, number of vertical levels, experiment ID and corresponding official references.

Model name	Ocean component	Horizontal resolution	Vertical levels	Experiment ID	Key reference
ACCESS-ESM1-5	MOM5	100 km	50	historical	(Ziehn et al., 2019)
AWI-CM-1-1-HR	FESOM 1.4	Unstructured (Ocean: ~25 km)	46	hist-1950	(Semmler et al., 2017)
AWI-CM-1-1-MR	FESOM 1.4	25 km	46	historical	(Semmler et al., 2018)
CanESM5	NEMO3.4.1	100 km	45	historical	(Swart et al., 2019)
CESM1-CAM5-SE-HR	POP2	10 km	62	hist-1950	(Hurrel et al., 2020a)
CESM1-CAM5-SE-LR	POP2	100 km	60	hist-1950	(Hurrel et al., 2020b)
CESM2	POP2	100 km	60	historical	(Danabasoglu, 2019)
CIESM	CIESM-OM	50 km	46	historical	(Huang, 2019)
CMCC-CM2-HR4	NEMO3.6	25 km	50	historical	(Scoccimarro et al., 2020)
CMCC-CM2-SR5	NEMO3.6	100 km	50	historical	(Lovato & Peano, 2020)
CNRM-CM6-1	NEMO3.6	100 km	75	historical	(Voldoire, 2018)
CNRM-CM6-1-HR	NEMO3.6	25 km	75	historical	(Voldoire, 2019)
FGOALS-f3-H	LICOM3.0	10 km	55	hist-1950	(Yu, 2020)
FIO-ESM-2-0	POP2-W	100 km	60	historical	(Song et al., 2019)
ICON-ESM-LR	ICON-O	Triangular Grid (Ocean: ~50 km)	40	historical	(Lorenz et al.,2021b)

Model name	Ocean component	Horizontal resolution	Vertical levels	Experiment ID	Key reference
IPSL-CM6A-LR	NEMO-OPA	100 km	75	historical	(Boucher et al., 2018)

2.2 Methods

The classical definition of AABW is a neutral density greater than 28.27 kg·m^{-3} (Orsi et al., 1999). The salinities of Weddell Sea Bottom Water (WSBW), Ross Sea Bottom Water (RSBW), and Adélie Land Bottom Water (ALBW) are 34.650 ± 0.005, 34.695 ± 0.005, and 34.683 ± 0.005, respectively (Pardo et al., 2012) . Due to the close spatial distribution of Prydz Bay Bottom Water (Solodoch et al., 2022), we combine it with Weddell Sea Bottom Water and refer to the merged water mass as Weddell–Prydz Bottom Water (WPBW). Given that one standard deviation (0.005) corresponds to a relatively narrow salinity range, especially considering the study area spans from the Antarctic coast to 50°S, where water mass transport and mixing can cause slight salinity variations, we adopt two standard deviations to define the salinity ranges of AABW originating from these three source regions. For instance, the salinity range for WPBW is defined as 34.640–34.660. Potential temperature, a commonly used physical parameter in oceanography, is not employed in this definition due to its substantial temporal and spatial variability, which could easily render the classification invalid. Moreover, AABW is characterized by low temperatures, and under such conditions, sea water density is predominantly controlled by salinity, with temperature playing a relatively minor role. Therefore, in this study, the two key parameters used to distinguish different types of AABW are neutral density and salinity (Table 2).

Based on the spatial distribution of regionally sourced AABW (Solodoch et al., 2022), Here WPBW is confined to the region between 60°W and 70°E, RSBW to the regions from 160°E to 180°E and from 180°W to 60°W, and ALBW to the region between 70°E and 160°E. The analysis is performed at 4000 m depth, a depth commonly used to quantify abyssal ocean changes (Li et al., 2023; Purkey & Johnson, 2010), as well as in the near-bottom layer. The 4000 m level is used to interpolate each dataset onto the reanalysis vertical grid. For the near bottom analysis, the deepest valid data layer of each dataset is considered representative of the near bottom, provided that the two layers above also contain valid data to avoid singular values. Slight discrepancies may exist among different model datasets.

Table 2. Classification and definition of AABW subtypes in this study.

	WPBW	RSBW	ALBW
Neutral density (kg m^{-3})	≥28.27		
Salinity (psu)	34.640 ~ 34.660	34.693 ~ 34.705	34.673 ~ 34.685

3 Results

3.1 WOA23 observational data

At the 4000 m layer, RSBW is characterized by relatively high potential temperature and salinity, and is predominantly distributed in the eastern Ross Sea, Amundsen Sea, and Bellingshausen Sea within the 70°S–60°S latitudinal band. In contrast, WPBW exhibits lower potential temperature and salinity, and is mainly found in the Weddell Sea, also within 70°S–60°S. ALBW exhibits intermediate thermohaline properties and a fragmented spatial distribution, primarily occurring between 75°E–105°E and 105°E–150°E along the Antarctic continental margin, within the 60°S–50°S latitude range (Figure 1a, c).

At the near bottom water layer, the overall distribution of AABW is consistent with previous studies (Orsi et al., 1999; Purkey et al., 2018), with RSBW exhibiting characteristically higher potential temperature and salinity, and WPBW showing lower values. However, notable differences emerge among the AABW subtypes compared to the 4000 m layer: the spatial extent of RSBW has increased markedly, particularly in northward extension in the Bellingshausen Sea and westward extension in the Ross Sea. WPBW has also expanded, with a pronounced northward extension near 30°E. (Figure 1b, d).

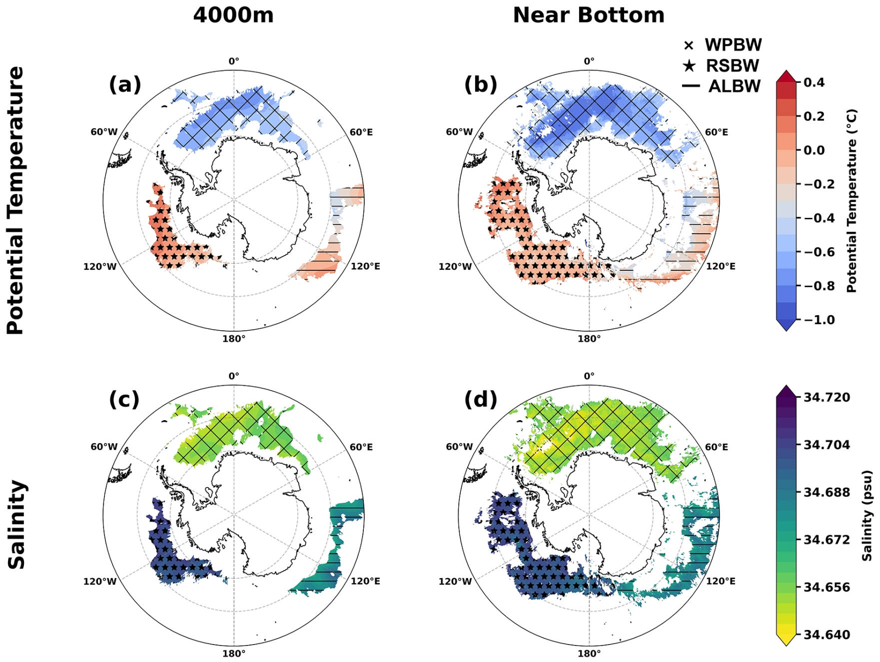

Figure 1. Distribution of AABW subtypes from the 1991–2020 climatology based on WOA2023. (a) and (b) show the potential temperature distribution of the defined AABW subtypes at the 4000 m layer and the near bottom layer, respectively. (c) and (d) present the salinity distribution of the defined AABW subtypes at the 4000 m layer and the near bottom layer, respectively. Symbols for the different AABW subtypes are shown in the legend.

3.2 Reanalysis data

At the 4000 m layer, the ensemble reanalysis data indicate that, Consistent with WOA23 observation, RSBW exhibits relatively high potential temperature and salinity, while WPBW exhibits cooler and fresher signature. Moreover, the spatial extent of RSBW in the reanalysis data is reduced, primarily in the western and central Amundsen Sea, while ALBW is more extensive than in WOA23, forming a continuous band between 75°E and 150°E (Figure 2a, c). In contrast, WPBW closely matches the spatial distribution in WOA23.

At the near bottom layer, the reanalysis data further show that, consistent with the observation-based AABW distribution, RSBW is also characterized by relatively elevated potential temperature and salinity, whereas WPBW exhibits relatively lower temperature and salinity. The spatial extent of RSBW is also markedly reduced, primarily confined to the eastern Ross Sea and the central-western Amundsen Sea. Similarly, the distribution of WPBW is more constrained relative to the WOA23 data, particularly with reduced northward penetration. In contrast, ALBW covers a much broader area than in the WOA23 data, extending from the Antarctic continental margin nearly to 50°S within the longitudinal band of 75°E–150°E (Figure 2b, d).

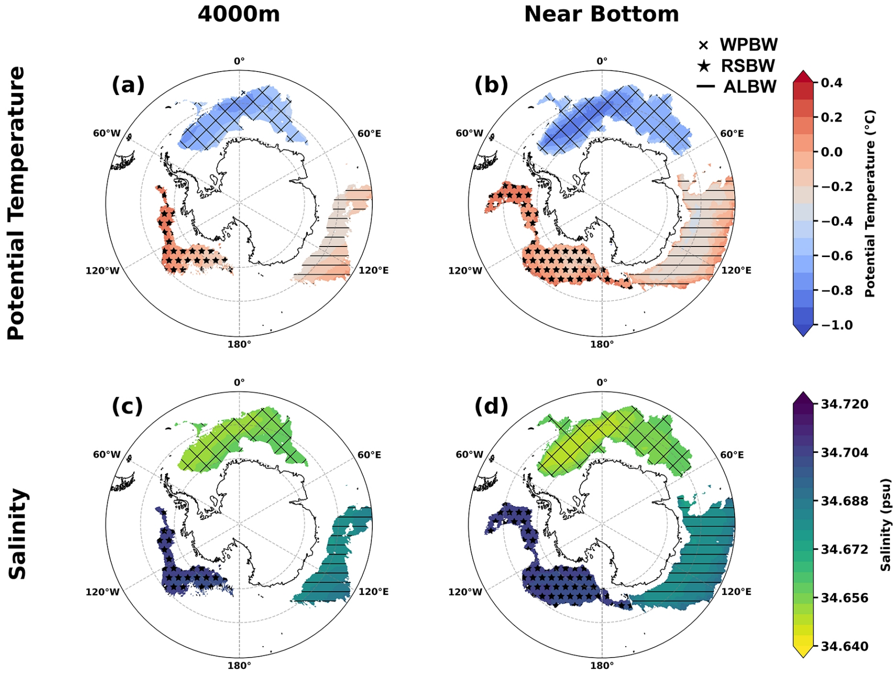

Figure 2. Distribution of AABW subtypes from 1993 to 1998 based on the reanalysis dataset (GLOBAL_MULTIYEAR_PHY_ENS_001_031). (a) and (b) show the distribution of potential temperature for different types of AABW defined at the 4000 m and near bottom layer, respectively. (c) and (d) show the distribution of salinity for different types of AABW defined at the 4000 m and near bottom layer, respectively. Symbols for the different AABW subtypes are shown in the legend.

3.3 Model outputs

As highlighted by Heuzé (2021), the performance of climate models in simulating AABW might be enhanced through two main approaches: increasing model resolution and improving the parameterization of complex physical processes. Ocean models with resolutions finer than 25 km can begin to describe the core structure of mesoscale eddies in open oceans (Chassignet & Xu, 2021; Hewitt et al., 2020). However, in some cases, coarser-resolution models may better represent certain physical process parameterizations. Based on these considerations, CMIP6 models used in this study are classified by the resolution of their ocean components into low resolution (100 km), moderate resolution (25–50 km), and high resolution (10 km). The analysis is also conducted at the 4000 m and near-bottom layer, respectively.

3.3.1 At the 4000 m layer

Among the eight selected low-resolution models, only CanESM5, CESM1-CAM5-SE-LR, and IPSL-CM6A-LR partially capture the distribution of AABW subtypes. Specifically, in the CanESM5 model, RSBW is mainly confined to the eastern Ross Sea and a narrow band of the Amundsen and Bellingshausen Seas, while WPBW is extended well into the western Indian sector of the Antarctic. However, ALBW is not captured. The CESM1-CAM5-SE-LR model captures the AABW subtypes remarkably well, reproducing the spatial patterns observed in WOA23 and reanalysis data. In contrast, the IPSL-CM6A-LR model shows a sparse RSBW in the Ross Sea, WPBW located mainly in the western Indian sector, and a narrow presence of ALBW along the Antarctic continental margin between 75°E and 150°E (Figure 3).

Within the six selected moderate resolution models, nearly all fail to reproduce the AABW subtypes, though the AWI-CM-1-1-HR model shows a minimal representation of the ALBW subtype (Figure 3).

Among the two selected high-resolution models, the CESM1-CAM5-SE-HR model captures the Atlantic portion of WPBW relatively well, yet it fails to capture other AABW subtypes. In contrast, the FGOALS-f3-H model represents RSBW, WPBW, and ALBW in a scattered manner, showing substantial deviations from the spatial patterns observed in WOA23 and reanalysis data (Figure 3).

https://doi.org/10.5194/egusphere-2026-978
Preprint. Discussion started: 4 March 2026

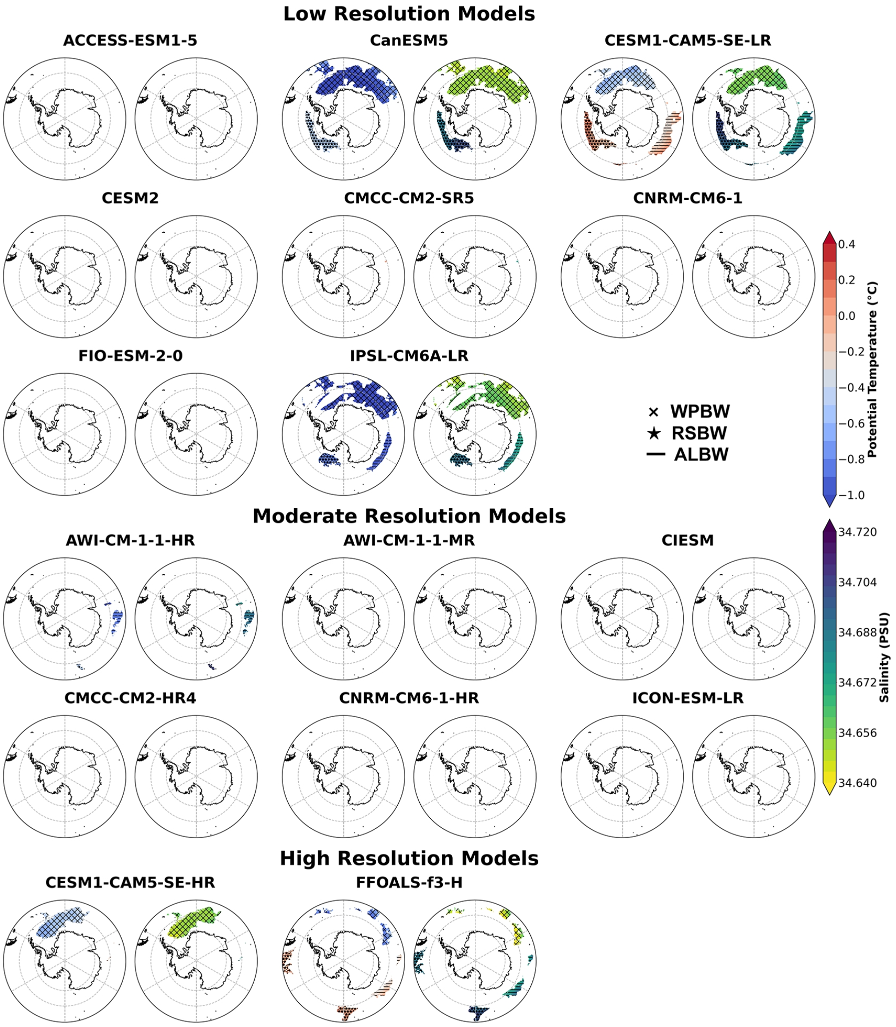

Figure 3. The potential temperature and salinity of AABW subtypes at the 4000m layer based on CMIP6 models. Symbols for the different AABW subtypes are shown in the legend.

3.3.2 At the near bottom layer

Among the low-resolution models, CanESM5, CESM1-CAM5-SE-LR, and IPSL-CM6A-LR exhibit a discernible bottom water distribution, while CMCC-CM2-SR5 shows only a minimal presence of ALBW. In the CanESM5 model, RSBW is distributed from the central Ross Sea to the western Amundsen Sea, while WPBW occupies an extensive area spanning nearly the entire Weddell Sea and the western Indian sector of the Antarctic, as well as the region to its north. However, no ALBW is found. The CESM1-CAM5-SE-LR model demonstrates a reasonably representation of the different AABW subtypes, reproducing the distribution patterns of each type as reflected in the WOA23. In the IPSL-CM6A-LR model, WPBW appears in the northern Weddell Sea and the western Indian sector but is absent from the central core region, while ALBW is reasonably represented along the Antarctic continental margin between 75°E and 160°E (Figure 4).

Of the moderate resolution models, almost none can capture the AABW subtypes, though the AWI-CM-1-1-HR model shows a limited extent of ALBW, slightly more extensive than that depicted at the 4000m depth (Figure 4).

Among the high-resolution models, the CESM1-CAM5-SE-HR model captures WPBW relatively well but fails to reproduce the other AABW subtypes. The distribution of AABW subtypes in the FGOALS-f3-H model is similar to its pattern at 4000m, characterized by a sparse and fragmented structure (Figure 4).

https://doi.org/10.5194/egusphere-2026-978
Preprint. Discussion started: 4 March 2026

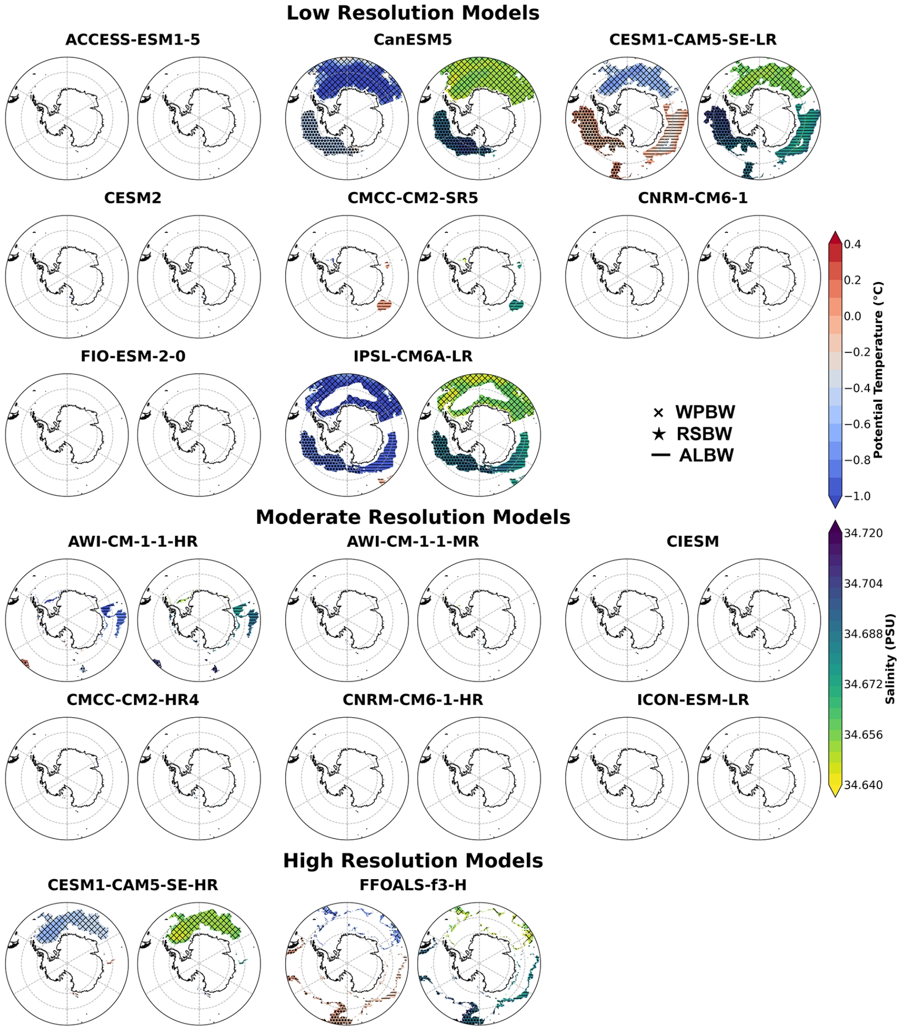

Figure 4. The potential temperature and salinity of AABW subtypes at the near bottom layer based on CMIP6 models. Symbols for the different AABW subtypes are shown in the legend.

3.3.3 Influence of overflow parameterization

The Ross Sea and Weddell Sea are two key regions for the formation of AABW via overflows of dense shelf water due to a combination of brine rejection and ocean and ice shelf interaction processes. However, due to limited model resolution, global

https://doi.org/10.5194/egusphere-2026-978
Preprint. Discussion started: 4 March 2026

climate models are generally unable to explicitly resolve these processes (Heuzé, 2021; Mensah et al., 2021) . To address this issue, the Climate Variability and Predictability (CLIVAR) Climate Process Team developed an overflow parameterization for the Parallel Ocean Program version 2 (Brinkgreve & Kumarswamy, 2008; Danabasoglu et al., 2010, 2012). This scheme is activated when the density of shelf water exceeds a predefined threshold, channeling dense shelf water through an artificial conduit directly into the deep ocean basin, thereby bypassing the explicit representation of the descent along topographic slopes. Using this process, water mass properties remain largely unchanged, in contrast to the large changes in water mass properties caused by excessive mixing in kilometer-scale climate models. The parameterization has been shown to perform effectively in model simulations (Brinkgreve & Kumarswamy, 2008; Heuzé, 2021). In this study, the models that adopt this scheme include CESM1-CAM5-SE-LR, CESM1-CAM5-SE-HR, CESM2 and FIO-ESM-2-0 (note that the remaining models do not clearly indicate the use of analogous parameterizations). Among the four models incorporating the overflow parameterization scheme, CESM2 and FIO-ESM-2-0 fail to represent all AABW subtypes, CESM1-CAM5-SE-HR only simulates ALBW subtype, and CESM1-CAM5-SE-LR successfully captures the three types of AABW, though the simulated spatial extent of ALBW is somewhat overestimated. In contrast, most models without this parameterization scheme fail to capture AABW subtypes. Exceptions are CanESM5 and IPSL-CM6A-LR, but their performance is markedly inferior to that of CESM1-CAM5-SE-LR (Figures 3 and 4).

A comparison of AABW simulations between CESM1-CAM5-SE-HR and CESM1-CAM5-SE-LR reveals that simply increasing the model resolution does not systematically improve the representation of AABW subtypes (Figures 3 and 4). One plausible explanation is that the physical parameterization schemes in the low-resolution model have been extensively tuned to achieve an optimal simulation state. If the high-resolution version continues to employ or only marginally adjusts the parameterizations originally designed for low resolution configurations, this scheme may become incompatible with the newly resolved dynamical processes, thereby introducing substantial differences (Roberts et al., 2018).

3.4 Model biases correction

We know that the models exhibit systematic biases in simulating potential temperature and salinity (Heuzé, 2021). To address this issue, a bias correction is applied to each model. Specifically, for each subtype region (e.g., WPBW, 60°W–70°E), the region-wide mean bias is calculated by subtracting the model's multi-year mean from the reanalysis mean, and this value is then subtracted from all grid points within that region.

After applying the correction for potential temperature and salinity, except CNRM-CM6-1-HR which exhibits no AABW signal in the near-bottom layer, all models can capture AABW subtypes to some extent, although its spatial distribution may differ from WOA23 and the reanalysis data (Figures 5–6).

At the 4000 m water layer, among the low-resolution models, ACCESS-ESM1-5, CESM1-CAM5-SE-LR, CMCC-CM2-SR5, and CNRM-CM6-1 show relatively good performance after the bias correction, generally consistent with the reanalysis and WOA23 data. However, the spatial extent of RSBW in CESM1-CAM5-SE-LR, CMCC-CM2-SR5, and CNRM-CM6-1 is somewhat reduced relative to WOA23. For the moderate resolution models, CIESM, CMCC-CM2-HR4, and ICON-ESM-LR perform relatively well with the bias correction. These models consistently simulate a more limited spatial extent of RSBW. WPBW is captured with reasonably well position and extent, while ALBW is confined within the longitudinal band of 75°E–135°E. Among the high-resolution models, CESM1-CAM5-SE-HR and FGOALS-f3-H are consistent with the observations after the bias correction, capturing all three subtypes of AABW. In CESM1-CAM5-SE-HR, RSBW and WPBW exhibit reduced spatial extent. In FGOALS-f3-H, both RSBW and ALBW have much smaller spatial coverage (Figure 5).

https://doi.org/10.5194/egusphere-2026-978
Preprint. Discussion started: 4 March 2026

At the near bottom layer, among the low-resolution models, only the ACCESS-ESM1-5 exhibits satisfactory performance after the bias correction. In contrast, the CESM1-CAM5-SE-LR model shows degraded performance after the correction, with ALBW only distributed along the margins and absent in the central part of the 75°E–150°E sector. Among the moderate resolution models, only CMCC-CM2-HR4 performs well with the correction, though RSBW is present in a smaller area, WPBW occupies a broader region in the Weddell Sea, and ALBW extends across the longitudinal band of 75°E–135°E, covering a larger area. As for the high-resolution models, both models fail to capture RSBW, though the bias-corrected CESM1-CAM5-SE-HR model captures WPBW and ALBW more accurately (Figure 6).

Overall, aside from CESM1-CAM5-SE-LR, which has good inherent simulation skill, only ACCESS-ESM1-5 and CMCC-CM2-HR4 demonstrate reliable performance after the correction at the 4000 m and near bottom layer.

https://doi.org/10.5194/egusphere-2026-978
Preprint. Discussion started: 4 March 2026

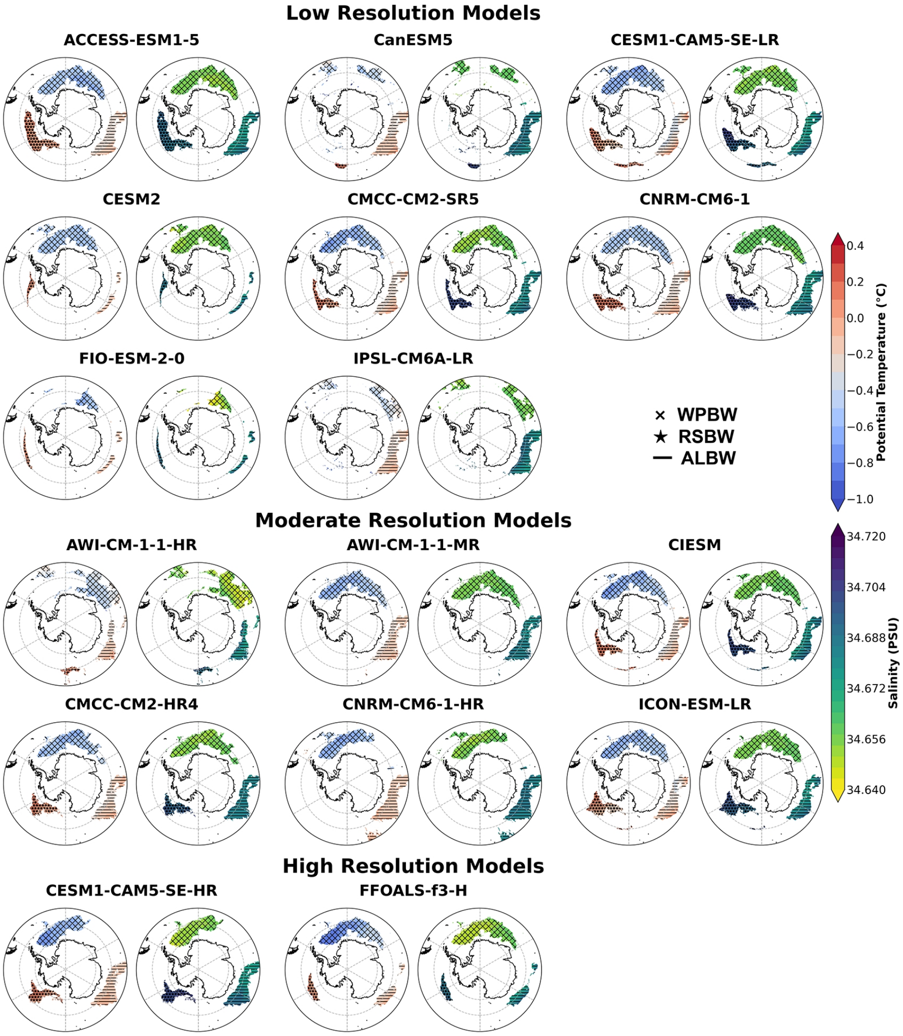

Figure 5. The bias-corrected potential temperature and salinity of AABW subtypes at the 4000m layer based on CMIP6 models. Symbols for the different AABW subtypes are shown in the legend.

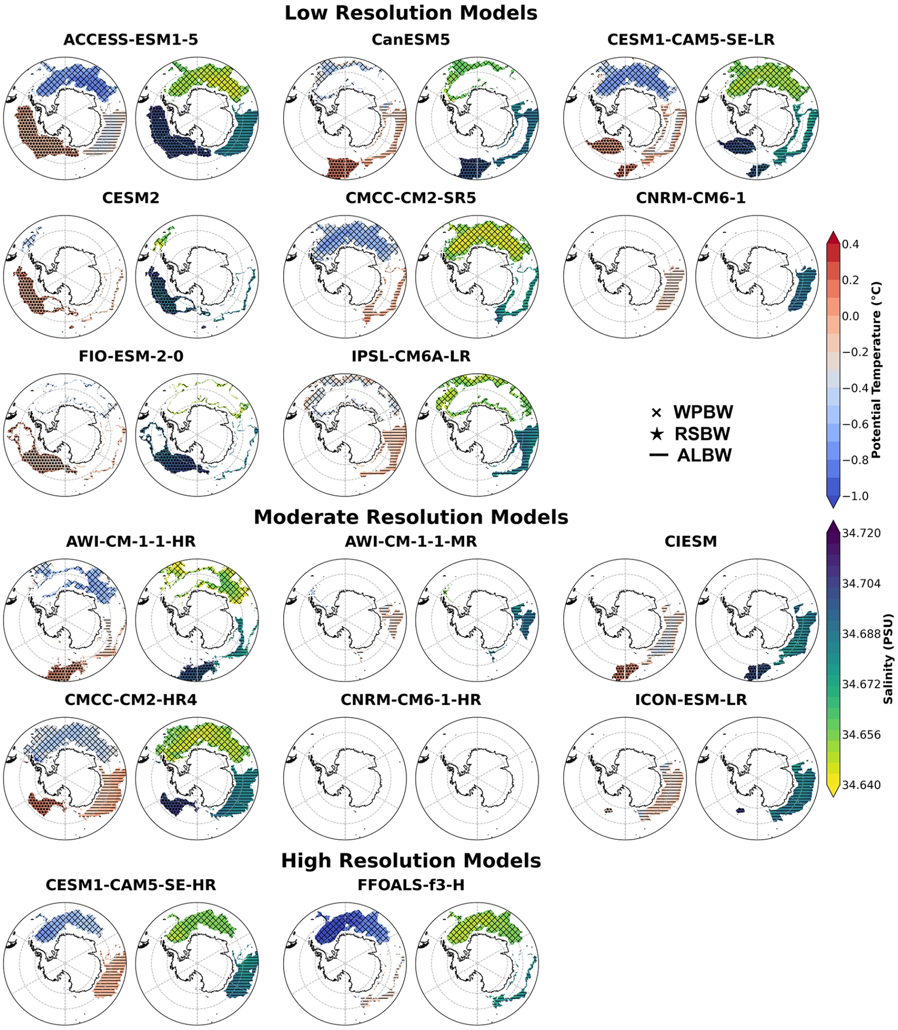

Figure 6. The bias-corrected potential temperature and salinity of AABW subtypes at the near bottom layer based on CMIP6 models. Symbols for the different AABW subtypes are shown in the legend.

4 Discussion: changes in the area of AABW subtypes

Previous assessments of AABW variability have primarily relied on sectional observations to estimate its spatial extent or volume within specific basins.

Multi-decadal hydrographic sections (e.g., A12, SR4, A23) show a persistent contraction in the area occupied by WSBW between 1995 and 2012 (Zhou et al., 2023) . High-resolution hydrographic observations reveal significant decadal-scale variability in AABW thickness in the Ross Sea. Near Cape Adare and along 150°E, AABW exhibited thinning from 1990 to 2011, followed by thickening until 2020, potentially due to a renewal event during 2018–2019 (Silvano et al., 2020). Similarly, repeated surveys along 170°E showed a ~ 70% reduction in RSBW ($\gamma^n \geq 28.30$ kg m^{-3}) area between 1992 and 2011, with a notable recovery by 2018 (Gunn et al., 2023). Additionally, repeat WOCE hydrographic sections along 140°E off the Adélie Coast document an overall reduction in the AABW area between 1993 and 2012 (van Wijk & Rintoul, 2014). While these in-situ measurement–based data provide relatively accurate assessments, their limited spatial coverage makes comprehensive monitoring of AABW challenging. The reanalysis and CMIP6 models, despite their inherent biases, can offer valuable supplementary information for these otherwise poorly observed areas. Furthermore, since this study introduces a new classification for different types of AABW, their respective area trends may also differ. Thus, built on our analyses in section 2 and 3, here we provide a brief analysis and comparison of the area changes for the newly defined AABW types, as represented by the reanalysis data and the CESM1-CAM5-SE-LR model, as well as the corrected ACCESS-ESM1-5 model and CMCC-CM2-HR4 model (Figure 7).

Based on the reanalysis data, although the area of RSBW does not exhibit a significant trend over the full period, it decreases significantly during 1998–2008 and 2013–2022 at both the 4000 m and bottom layers. In contrast, the area of WPBW shows a significant declining trend from 1998 to 2022, with an almost linear decrease particularly at the 4000 m layer. For ALBW, the 4000 m layer presents a fluctuating increase from 1993 to 2004, followed by reduced variability after 2004. At the near bottom layer, however, ALBW continues to fluctuate from 1993 to 2022, albeit with a higher climatological mean after 2003(Figure 7a, b). In contrast, the CESM1-CAM5-SE-LR model, which performs well in simulating the three AABW subtypes, exhibits a significant area contraction for all three AABW subtypes (RSBW, WPBW, and ALBW) throughout the entire period (Figures 7c, d). The ACCESS-ESM1-5 and CMCC-CM2-HR4, which have improved performance in simulating the AABW subtypes after the correction, also show declining trends for RSBW and WPBW. However, ALBW exhibits notable divergence. At the 4000 m layer, the area of ALBW remains quite stable in the bias-corrected ACCESS-ESM1-5 and CMCC-CM2-HR4 models. At the near bottom layer, CMCC-CM2-HR4 displays a distinct evolution characterized by an initial expansion followed by a quick decline (Figures 7c, d). It is noteworthy that, although the overall trend in AABW area is declining, the variation in the ALBW area in this study differs depending on the data source. In any case, these results underscore the necessity of further subdivision of AABW.

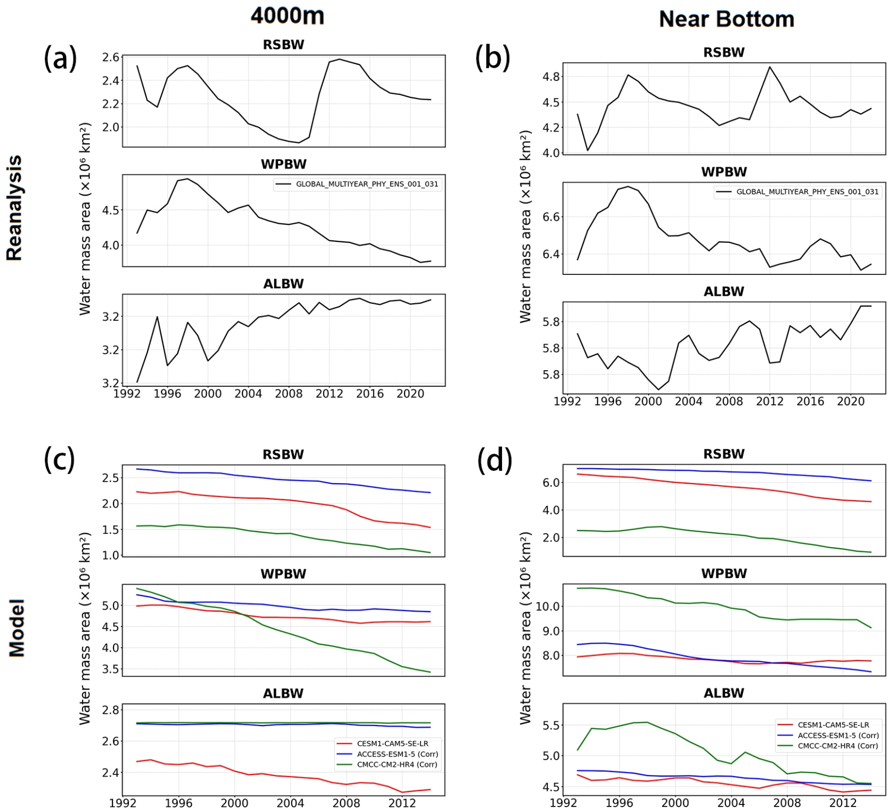

Figure 7. Changes in the area of AABW subtypes. Panels (a) and (b) present the area changes at the 4000 m and near bottom layer, respectively, derived from the reanalysis product (GLOBAL-MULTIYEAR-PHY-ENS-001-031). Panels (c) and (d) present the corresponding area changes at the 4000 m and near bottom layer based on output from the CESM1-CAM5-SE-LR model, as well as the bias-corrected ACCESS-ESM1-5 and CMCC-CM2-HR4 models.

5 Conclusion

Based on previous studies, this research proposes a new definition for reclassifying AABW and evaluates the performance of observational, reanalysis, and CMIP6 model outputs in capturing the reclassified AABW subtypes. The results indicate that the WOA23 data captures the distribution of WPBW, RSBW, and ALBW, and can be used as a benchmark. Compared to WAO23, the ensemble reanalysis data (GLOBAL_MULTIYEAR_PHY_ENS_001_031) well captures all three AABW subtypes, though it overestimates the spatial extent of ALBW. Most CMIP6 models require bias correction to reasonably simulate AABW subtype distributions. Among them, ACCESS-ESM1-5 and CMCC-CM2-HR4 show improved performance after the correction. In contrast, the CESM1-CAM5-SE-LR model can capture the distribution of all three AABW subtypes without the correction, which may be attributed in part to its explicit representation of overflows together with tuned simulation state. Furthermore, a comparison between CESM1-CAM5-SE-LR and its high-resolution counterpart (CESM1-CAM5-SE-HR) suggests that simply increasing model resolution does not necessarily lead to improved simulation of AABW subtypes.

Code and data availability

The datasets utilized in this study are publicly available from the sources indicated below: The World Ocean Atlas 2023 (WOA23) climatology data were obtained from the National Centers for Environmental Information (NCEI) at: https://www.ncei.noaa.gov/access/world-ocean-atlas-2023/.The global ocean ensemble physical reanalysis products are available via Copernicus Marine Service at: https://data.marine.copernicus.eu/product/GLOBAL_MULTIYEAR_PHY_ENS_001_031/services.The Coupled Model Intercomparison Project Phase 6 (CMIP6) data can be accessed through any Earth System Grid Federation (ESGF) portal; the outputs used in this paper were obtained from https://aims2.llnl.gov/.The code and processed data used for the analysis and plotting in this study are available at Zenodo via https://doi.org/10.5281/zenodo.18446787 (Chen et al., 2026).

Author contributions

JL conceptualized the study, supervised the research, and acquired the funding. SC performed the formal analysis, created the visualizations, and wrote the original draft of the manuscript. XH contributed to reviewing and editing the manuscript. All authors discussed the results and approved the final version.

Competing interests

The author declares no competing interests.

Acknowledgments

This research is supported by the National Key R&D Program of China (2024YFF0506600) and the Southern Marine Science and Engineering Guangdong Laboratory (Zhuhai) (SML2024SP023). We acknowledge the World Climate Research Programme (WCRP), which, through its Working Group on Coupled Modelling, coordinated and promoted CMIP6. We thank the climate modeling groups listed in Table 1 for producing and making available their model output, the Earth System Grid Federation (ESGF) for archiving the data and providing access, and the multiple funding agencies who support CMIP6 and ESGF. Additionally, we acknowledge the NOAA National Centers for Environmental Information (NCEI) for providing the World Ocean Atlas 2023 (WOA23) dataset, and the Copernicus Marine Service for making the global ocean ensemble physical reanalysis product publicly available.

Financial support

This research has been supported by the National Key R&D Program of China (2024YFF0506600) and the Southern Marine Science and Engineering Guangdong Laboratory (Zhuhai) (SML2024SP023).

References

Azaneu, M., Kerr, R., & Mata, M. M. (2014). Assessment of the representation of Antarctic Bottom Water properties in the ECCO2 reanalysis. *Ocean Science*, *10*(6), 923–946. https://doi.org/10.5194/os-10-923-2014

Bai, Y., Zhao, L., Xiao, J., & Lin, S. (2022). Contraction and warming of Antarctic Bottom Water in the Amundsen Sea. *Acta Oceanologica Sinica*, *41*(4), 68–79. https://doi.org/10.1007/s13131-021-1829-8

Boucher, O., Denvil, S., Levavasseur, G., Cozic, A., Caubel, A., Foujols, M.-A., Meurdesoif, Y., Cadule, P., Devilliers, M., Ghattas, J., Lebas, N., Lurton, T., Mellul, L., Musat, I., Mignot, J., & Cheruy, F. (2018). *IPSL IPSL-CM6A-LR model output prepared for CMIP6 CMIP historical*. Earth System Grid Federation. https://doi.org/10.22033/ESGF/CMIP6.5195

Brinkgreve, R. B. J., & Kumarswamy, S. (2008). Reference Manual Reference Manual. *Technology*, *1*(November), 720–766.

Burke, A., & Robinson, L. F. (2012). The southern ocean's role in carbon exchange during the last deglaciation. *Science*, *335*(6068), 557–561. https://doi.org/10.1126/science.1208163

Chassignet, E. P., & Xu, X. (2021). On the Importance of High-Resolution in Large-Scale Ocean Models. *Advances in Atmospheric Sciences*, *38*(10), 1621–1634.

https://doi.org/10.1007/s00376-021-0385-7

Chen, S., Liu, J., & Han, X. (2026). Code and processed data for "Characteristics of Antarctic Bottom Water in WOA, ocean ensemble reanalysis, and CMIP6 models" [Data set]. Zenodo. https://doi.org/10.5281/zenodo.18446787

Cheng, L., Zhu, J., Cowley, R., Boyer, T., & Wijffels, S. (2014). Time, probe type, and temperature variable bias corrections to historical expendable bathythermograph observations. *Journal of Atmospheric and Oceanic Technology*, *31*(8), 1793–1825. https://doi.org/10.1175/JTECH-D-13-00197.1

Danabasoglu, G. (2019). *NCAR CESM2 model output prepared for CMIP6 CMIP historical*. Earth System Grid Federation. https://doi.org/10.22033/ESGF/CMIP6.7627

Danabasoglu, G., Bates, S. C., Briegleb, B. P., Jayne, S. R., Jochum, M., Large, W. G., Peacock, S., & Yeager, S. G. (2012). The CCSM4 ocean component. *Journal of Climate*, *25*(5), 1361–1389. https://doi.org/10.1175/JCLI-D-11-00091.1

Danabasoglu, G., Large, W. G., & Briegleb, B. P. (2010). *Climate impacts of parameterized Nordic Sea overflows*. *115*(June), 1–29. https://doi.org/10.1029/2010JC006243

Gordon, A. L., Huber, B. A., Hellmer, H. H., & Ffield, A. (1993). Deep and Bottom Water of the Weddell Sea's Western Rim. *Science*, *262*(5130), 95–97. https://doi.org/10.1126/science.262.5130.95

Gouretski, V., & Koltermann, K. P. (2007). How much is the ocean really warming? *Geophysical Research Letters*, *34*(1), 1–5. https://doi.org/10.1029/2006GL027834

Gunn, K. L., Rintoul, S. R., England, M. H., & Bowen, M. M. (2023). Recent reduced abyssal overturning and ventilation in the Australian Antarctic Basin. *Nature Climate Change*, *13*(6), 537–544. https://doi.org/10.1038/s41558-023-01667-8

Han, X., Stewart, A. L., Chen, D., Janout, M., Liu, X., Wang, Z., & Gordon, A. L. (2024). Circum-Antarctic bottom water formation mediated by tides and topographic waves. *Nature Communications*, *15*(1). https://doi.org/10.1038/s41467-024-46086-1

Han, X., Stewart, A., Wang, Z., Yang, Q., Liu, C., & Chen, D. (2025). Tidal Effects on Antarctic Bottom Water Formation in a Changing Climate. *Journal of Geophysical Research: Oceans*, *130*(8), 1–18. https://doi.org/10.1029/2025JC022443

Heuzé, C. (2021). Antarctic Bottom Water and North Atlantic Deep Water in CMIP6 models.

Ocean Science, *17*(1), 59–90. https://doi.org/10.5194/os-17-59-2021

Hewitt, H. T., Roberts, M., Mathiot, P., Biastoch, A., Blockley, E., Chassignet, E. P., Fox-Kemper, B., Hyder, P., Marshall, D. P., Popova, E., Treguier, A. M., Zanna, L., Yool, A., Yu, Y., Beadling, R., Bell, M., Kuhlbrodt, T., Arsouze, T., Bellucci, A., … Zhang, Q. (2020). Resolving and Parameterising the Ocean Mesoscale in Earth System Models. *Current Climate Change Reports*, *6*(4), 137–152. https://doi.org/10.1007/s40641-020-00164-w

Huang, W. (2019). *THU CIESM model output prepared for CMIP6 CMIP historical*. Earth System Grid Federation. https://doi.org/10.22033/ESGF/CMIP6.8843

Hurrel, J., Holland, M., Gent, P., Ghan, S., Kay, J., Kushner, P., Lamarque, J.-F., Large, W. G., Lawrence, D., Lindsay, K., Lipscomb, W., Long, M., Mahowald, N. M., Marsh, D., Neale, R., Rasch, P. J., Vavrus, S. J., Vertenstein, M., Bader, D. C., … Marshall, S. (2020a). *NCAR CESM1-CAM5-SE-HR model output prepared for CMIP6 HighResMIP*. Earth System Grid Federation. https://doi.org/10.22033/ESGF/CMIP6.14220

Hurrel, J., Holland, M., Gent, P., Ghan, S., Kay, J., Kushner, P., Lamarque, J.-F., Large, W. G., Lawrence, D., Lindsay, K., Lipscomb, W., Long, M., Mahowald, N. M., Marsh, D., Neale, R., Rasch, P. J., Vavrus, S. J., Vertenstein, M., Bader, D. C., … Marshall, S. (2020b). *NCAR CESM1-CAM5-SE-LR model output prepared for CMIP6 HighResMIP hist-1950*. Earth System Grid Federation. https://doi.org/10.22033/ESGF/CMIP6.14295

Jackett, D. R., & Mcdougall, T. J. (1995). Minimal Adjustment of Hydrographic Profiles to Achieve Static Stability. *Journal of Atmospheric and Oceanic Technology*, *12*(2), 381–389. https://doi.org/https://doi.org/10.1175/1520-0426(1995)012<0381:MAOHPT>2.0.CO;2

Johnson, G. C., Purkey, S. G., & Toole, J. M. (2008). Reduced antarctic meridional overturning circulation reaches the North Atlantic ocean. *Geophysical Research Letters*, *35*(22), 1–5. https://doi.org/10.1029/2008GL035619

J.R. Reagan, D. Seidov, Z. Wang, D. Dukhovskoy, T.P. Boyer, R.A. Locarnini, O.K. Baranova, A.V. Mishonov, H.E. Garcia, C. Bouchard, S.L. Cross, & C.R. Paver. (2024). *NOAA Atlas NESDIS 90 WORLD OCEAN ATLAS 2023 Volume 2: Salinity*. *2*(February). https://doi.org/10.25923/70qt-9574

Lellouche, J. M., Le Galloudec, O., Drévillon, M., Régnier, C., Greiner, E., Garric, G., Ferry, N., Desportes, C., Testut, C. E., Bricaud, C., Bourdallé-Badie, R., Tranchant, B., Benkiran, M.,

https://doi.org/10.5194/egusphere-2026-978
Preprint. Discussion started: 4 March 2026

Drillet, Y., Daudin, A., & De Nicola, C. (2013). Evaluation of global monitoring and forecasting systems at Mercator Océan. *Ocean Science*, *9*(1), 57–81. https://doi.org/10.5194/os-9-57-2013

Levitus, S., Antonov, J. I., Boyer, T. P., Locarnini, R. A., Garcia, H. E., & Mishonov, A. V. (2009). Global ocean heat content 1955-2008 in light of recently revealed instrumentation problems. *Geophysical Research Letters*, *36*(7), 1–5. https://doi.org/10.1029/2008GL037155

Li, Q., England, M. H., Hogg, A. M. C., Rintoul, S. R., & Morrison, A. K. (2023). Abyssal ocean overturning slowdown and warming driven by Antarctic meltwater. *Nature*, *615*(7954), 841–847. https://doi.org/10.1038/s41586-023-05762-w

Locarnini, R. A., Mishonov, A. V, Baranova, O. K., Reagan, J. R., Boyer, T. P., Seidov, D., Wang, Z., Garcia, H. E., Bouchard, C., Cross, S. L., Paver, C. R., & Dukhovskoy, D. (2024). World Ocean Atlas 2023, Volume 1: Temperature. *NOAA Atlas NESDIS 89*, *89*(February), 52. https://doi.org/10.25923/54bh-1613

Lorenz, S., Jungclaus, J., Schmidt, H., Haak, H., Reick, C., Schupfner, M., Wachsmann, F., Gayler, V., de Vrese, P., Raddatz, T., Mauritsen, T., von Storch, J.-S., Brovkin, V., Claussen, M., Crueger, T., Fiedler, S., Hagemann, S., Hohenegger, C., Jahns, T., … Ilyina, T. (2021). *MPI-M ICON-ESM-LR model output prepared for CMIP6 CMIP historical*. Earth System Grid Federation. https://doi.org/10.22033/ESGF/CMIP6.6593

Lovato, T., & Peano, D. (2020). *CMCC CMCC-CM2-SR5 model output prepared for CMIP6 CMIP historical*. Earth System Grid Federation. https://doi.org/10.22033/ESGF/CMIP6.3825

Marinov, I., Gnanadesikan, A., Toggweiler, J. R., & Sarmiento, J. L. (2006). The Southern Ocean biogeochemical divide. *Nature*, *441*(7096), 964–967. https://doi.org/10.1038/nature04883

Mensah, V., Nakayama, Y., Fujii, M., Nogi, Y., & Ohshima, K. I. (2021). Dense water downslope flow and AABW production in a numerical model: Sensitivity to horizontal and vertical resolution in the region off Cape Darnley polynya. *Ocean Modelling*, *165*(October 2020), 101843. https://doi.org/10.1016/j.ocemod.2021.101843

Ohshima, K. I., Fukamachi, Y., Williams, G. D., Nihashi, S., Roquet, F., Kitade, Y., Tamura, T., Hirano, D., Herraiz-Borreguero, L., Field, I., Hindell, M., Aoki, S., & Wakatsuchi, M. (2013). Antarctic Bottom Water production by intense sea-ice formation in the Cape Darnley polynya. *Nature Geoscience*, *6*(3), 235–240. https://doi.org/10.1038/ngeo1738

Orsi, A. H., Johnson, G. C., & Bullister, J. L. (1999). Circulation, mixing, and production of Antarctic Bottom Water. *Progress in Oceanography*, *43*(1), 55–109. https://doi.org/10.1016/S0079-6611(99)00004-X

Pardo, P. C., Pérez, F. F., Velo, A., & Gilcoto, M. (2012). Water masses distribution in the Southern Ocean: Improvement of an extended OMP (eOMP) analysis. *Progress in Oceanography*, *103*, 92–105. https://doi.org/10.1016/j.pocean.2012.06.002

Purkey, S. G., & Johnson, G. C. (2010). Warming of global abyssal and deep Southern Ocean waters between the 1990s and 2000s: Contributions to global heat and sea level rise budgets. *Journal of Climate*, *23*(23), 6336–6351. https://doi.org/10.1175/2010JCLI3682.1

Purkey, S. G., & Johnson, G. C. (2013). Antarctic bottom water warming and freshening: Contributions to sea level rise, ocean freshwater budgets, and global heat gain. *Journal of Climate*, *26*(16), 6105–6122. https://doi.org/10.1175/JCLI-D-12-00834.1

Purkey, S. G., Smethie, W. M., Gebbie, G., Gordon, A. L., Sonnerup, R. E., Warner, M. J., & Bullister, J. L. (2018). A synoptic view of the ventilation and circulation of antarctic bottom water from chlorofluorocarbons and natural tracers. *Annual Review of Marine Science*, *10*, 503–527. https://doi.org/10.1146/annurev-marine-121916-063414

Rintoul, S. R. (2018). The global influence of localized dynamics in the Southern Ocean. *Nature*, *558*(7709), 209–218. https://doi.org/10.1038/s41586-018-0182-3

Roberts, M. J., Vidale, P. L., Senior, C., Hewitt, H. T., Bates, C., Berthou, S., Chang, P., Christensen, H. M., Danilov, S., Demory, M. E., Griffies, S. M., Haarsma, R., Jung, T., Martin, G., Minobe, S., Ringler, T., Satoh, M., Schiemann, R., Scoccimarro, E., … Wehner, M. F. (2018). The benefits of global high resolution for climate simulation process understanding and the enabling of stakeholder decisions at the regional scale. *Bulletin of the American Meteorological Society*, *99*(11), 2341–2359. https://doi.org/10.1175/BAMS-D-15-00320.1

Schmidt, C., Morrison, A. K., & England, M. H. (2023). Wind– and Sea-Ice–Driven Interannual Variability of Antarctic Bottom Water Formation. *Journal of Geophysical Research: Oceans*, *128*(6). https://doi.org/10.1029/2023JC019774

Scoccimarro, E., Bellucci, A., & Peano, D. (2020). *CMCC CMCC-CM2-HR4 model output prepared for CMIP6 CMIP historical*. Earth System Grid Federation.

https://doi.org/10.22033/ESGF/CMIP6.3823

Semmler, T., Danilov, S., Rackow, T., Sidorenko, D., Barbi, D., Hegewald, J., Sein, D., Wang, Q., & Jung, T. (2018). *AWI AWI-CM1.1MR model output prepared for CMIP6 CMIP historical*. Earth System Grid Federation. https://doi.org/10.22033/ESGF/CMIP6.2686

Semmler, T., Danilov, S., Rackow, T., Sidorenko, D., Hegewald, J., Sein, D., Wang, Q., & Jung, T. (2017). *AWI AWI-CM1.1HR model output prepared for CMIP6 HighResMIP hist-1950*. Earth System Grid Federation. https://doi.org/10.22033/ESGF/CMIP6.2676

Silvano, A., Foppert, A., Rintoul, S. R., Holland, P. R., Tamura, T., Kimura, N., Castagno, P., Falco, P., Budillon, G., Haumann, F. A., Naveira Garabato, A. C., & Macdonald, A. M. (2020). Recent recovery of Antarctic Bottom Water formation in the Ross Sea driven by climate anomalies. *Nature Geoscience*, *13*(12), 780–786. https://doi.org/10.1038/s41561-020-00655-3

Silvano, A., Purkey, S., Gordon, A. L., Castagno, P., Stewart, A. L., Rintoul, S. R., Foppert, A., Gunn, K. L., Herraiz-Borreguero, L., Aoki, S., Nakayama, Y., Naveira Garabato, A. C., Spingys, C., Akhoudas, C. H., Sallée, J. B., de Lavergne, C., Abrahamsen, E. P., Meijers, A. J. S., Meredith, M. P., … Lee, W. S. (2023). Observing Antarctic Bottom Water in the Southern Ocean. *Frontiers in Marine Science*, *10*(December), 1–30. https://doi.org/10.3389/fmars.2023.1221701

Silvano, A., Rintoul, S. R., Peña-Molino, B., Hobbs, W. R., Van Wijk, E., Aoki, S., Tamura, T., & Williams, G. D. (2018). Freshening by glacial meltwater enhances melting of ice shelves and reduces formation of Antarctic Bottom Water. *Science Advances*, *4*(4), 1–12. https://doi.org/10.1126/sciadv.aap9467

Solodoch, A., Stewart, A. L., Hogg, A. M. C., Morrison, A. K., Kiss, A. E., Thompson, A. F., Purkey, S. G., & Cimoli, L. (2022). How Does Antarctic Bottom Water Cross the Southern Ocean? *Geophysical Research Letters*, *49*(7), 1–11. https://doi.org/10.1029/2021GL097211

Song, Z., Qiao, F., Bao, Y., Shu, Q., Song, Y., & Yang, X. (2019). *FIO-QLNM FIO-ESM2.0 model output prepared for CMIP6 CMIP historical*. Earth System Grid Federation. https://doi.org/10.22033/ESGF/CMIP6.9199

Storto, A., & Masina, S. (2016). C-GLORSv5: An improved multipurpose global ocean eddy-permitting physical reanalysis. *Earth System Science Data*, *8*(2), 679–696.

https://doi.org/10.5194/essd-8-679-2016

Swart, N. C., Cole, J. N. S., Kharin, V. V, Lazare, M., Scinocca, J. F., Gillett, N. P., Anstey, J., Arora, V., Christian, J. R., Jiao, Y., Lee, W. G., Majaess, F., Saenko, O. A., Seiler, C., Seinen, C., Shao, A., Solheim, L., von Salzen, K., Yang, D., … Sigmond, M. (2019). *CCCma CanESM5 model output prepared for CMIP6 CMIP historical*. Earth System Grid Federation. https://doi.org/10.22033/ESGF/CMIP6.3610

Uotila, P., Goosse, H., Haines, K., Chevallier, M., Barthélemy, A., Bricaud, C., Carton, J., Fučkar, N., Garric, G., Iovino, D., Kauker, F., Korhonen, M., Lien, V. S., Marnela, M., Massonnet, F., Mignac, D., Peterson, K. A., Sadikni, R., Shi, L., … Zhang, Z. (2019). An assessment of ten ocean reanalyses in the polar regions. In *Climate Dynamics* (Vol. 52, Issues 3–4). Springer Berlin Heidelberg. https://doi.org/10.1007/s00382-018-4242-z

van Wijk, E. M., & Rintoul, S. R. (2014). Freshening drives contraction of Antarctic Bottom Water in the Australian Antarctic Basin. *Geophysical Research Letters*, *41*(5), 1657–1664. https://doi.org/https://doi.org/10.1002/2013GL058921

Voldoire, A. (2018). *CMIP6 simulations of the CNRM-CERFACS based on CNRM-CM6-1 model for CMIP experiment historical*. Earth System Grid Federation. https://doi.org/10.22033/ESGF/CMIP6.4066

Voldoire, A. (2019). *CNRM-CERFACS CNRM-CM6-1-HR model output prepared for CMIP6 CMIP historical*. Earth System Grid Federation. https://doi.org/10.22033/ESGF/CMIP6.4067

Williams, G. D., Bindoff, N. L., Marsland, S. J., & Rintoul, S. R. (2008). Formation and export of dense shelf water from the Adélie depression, East Antarctica. *Journal of Geophysical Research: Oceans*, *113*(4), 1–12. https://doi.org/10.1029/2007JC004346

YU, Y. (2020). *CAS FGOALS-f3-H model output prepared for CMIP6 HighResMIP hist-1950*. Earth System Grid Federation. https://doi.org/10.22033/ESGF/CMIP6.3316

Zhang, S., Wu, Y., Cai, W. J., Cai, W., Feely, R. A., Wang, Z., Tanhua, T., Wang, Y., Liu, C., Li, X., Yang, Q., Ding, M., Xu, Z., Kerr, R., Luo, Y., Cheng, X., Chen, L., & Qi, D. (2023). Transport of Anthropogenic Carbon From the Antarctic Shelf to Deep Southern Ocean Triggers Acidification. *Global Biogeochemical Cycles*, *37*(12), 1–17. https://doi.org/10.1029/2023GB007921

Zhou, S., Meijers, A. J. S., Meredith, M. P., Abrahamsen, E. P., Holland, P. R., Silvano, A., Sallée, J.

B., & Østerhus, S. (2023). Slowdown of Antarctic Bottom Water export driven by climatic wind and sea-ice changes. *Nature Climate Change*, *13*(7), 701–709. https://doi.org/10.1038/s41558-023-01695-4

Ziehn, T., Chamberlain, M., Lenton, A., Law, R., Bodman, R., Dix, M., Wang, Y., Dobrohotoff, P., Srbinovsky, J., Stevens, L., Vohralik, P., Mackallah, C., Sullivan, A., O'Farrell, S., & Druken, K. (2019). *CSIRO ACCESS-ESM1.5 model output prepared for CMIP6 CMIP historical*. Earth System Grid Federation. https://doi.org/10.22033/ESGF/CMIP6.4272

Zuo, H., Balmaseda, M. A., Tietsche, S., Mogensen, K., & Mayer, M. (2019). The ECMWF operational ensemble reanalysis-analysis system for ocean and sea ice: A description of the system and assessment. *Ocean Science*, *15*(3), 779–808. https://doi.org/10.5194/os-15-779-2019